Letter

Experiments on the dynamics and scaling of spontaneous-magnetic-field saturation in laser-produced plasmas

G. D. Sutcliffe,[1] J. A. Pearcy,[1] T. M. Johnson,[1] P. J. Adrian,[1] N. V. Kabadi,[1] B. Pollock,[2] J. D. Moody,[2] R. D. Petrasso,[1] and C. K. Li[1]

[1]*Plasma Science and Fusion Center, Massachusetts Institute of Technology, Cambridge, Massachusetts 02139, USA*

[2]*Lawrence Livermore National Laboratory, Livermore, California 94550, USA*

(Received 15 July 2021; revised 29 January 2022; accepted 16 May 2022; published 27 June 2022)

In laser-produced high-energy-density plasmas, large-scale strong magnetic fields are spontaneously generated by the Biermann battery effects when temperature and density gradients are misaligned. Saturation of the magnetic field takes place when convection and dissipation balance field generation. While theoretical and numerical modeling provide useful insight into the saturation mechanisms, experimental demonstration remains elusive. In this letter, we report an experiment on the saturation dynamics and scaling of Biermann battery magnetic field in the regime where plasma convection dominates. With time-gated charged-particle radiography and time-resolved Thomson scattering, the field structure and evolution as well as corresponding plasma conditions are measured. In these conditions, the spatially resolved magnetic fields are reconstructed, leading to a picture of field saturation with a scaling of $B \sim 1/L_{\mathrm{T}}$ for a convectively dominated plasma, a regime where the temperature gradient scale (L_{T}) exceeds the ion skin depth.

DOI: 10.1103/PhysRevE.105.L063202

Understanding the saturation mechanisms in magnetic field generation is a challenging undertaking essential to basic plasma physics. The generation, transport, and dissipation of spontaneous magnetic fields in plasmas are important physics issues fundamental to a large variety of frontier research areas from astrophysics [1,2] to laboratory plasmas [3–5]. In these environments, large-scale magnetic fields are self-generated when there are misaligned plasma temperature and density gradients ($\partial\mathbf{B}/\partial t \propto \nabla T_e \times \nabla n_e$), called the *Biermann battery* effect [6]. The Biermann fields are thought to be the critical seed fields responsible for magnetizing astrophysical background and affecting the structure and dynamics of many important astrophysical phenomena [1,2]. In laboratory experiments, such fields can be generated by laser-plasma interactions [5,7–11] which have important implications in broader research areas, including inertial confinement fusion [12,13] and scaled laboratory studies of astrophysical systems [14–17].

Plasmas produced by lasers impinging on solid material have high temperature and density and as a result are typically in the regime labeled high-energy density (HED), generally defined as pressure $>$ 1 MBar. In a two-fluid plasma model, the dynamics of the large-scale spontaneous magnetic fields are described by combining the Faraday equation with the generalized Ohm's law [5,18–20]:

$$\frac{\partial \mathbf{B}}{\partial t} = \frac{c(\nabla T_e \times \nabla n_e)}{e n_e} + \nabla \times (\mathbf{v} \times \mathbf{B}) - \frac{\eta c^2}{4\pi}\nabla^2 \mathbf{B}, \qquad (1)$$

where $\mathbf{v}$ is fluid velocity, $\eta \propto Z \ln\Lambda\, T_e^{-3/2}$ is plasma resistivity, and n_e and T_e are electron density and temperature, respectively. While several physics processes act as sources and sinks for spontaneous magnetic fields in plasmas, outlined in Eq. (1) are the dominant factors in the nonrelativistic hydrodynamic approximation. Authors of previous work [5,20] provided justification for ignoring terms related to high-intensity effects which manifest in short pulse ($<$ 100 ps) lasers. The first term on the right in Eq. (1) is the previously mentioned Biermann battery source term. The sinks are due to fluid convection (second term) and the resistive dissipation (third term). The saturation of spontaneous magnetic fields in plasmas results from balancing of these physical processes, leading to a quasi-equilibrium state where the global field ceases to grow. To evaluate their relative contributions, the resistive term compares with the convection term as $(\eta c^2/4\pi v L)$ [5,18–20] ($\sim 10^{-3}$ for low Z, 1 keV plasmas with length scale = 1 mm). The Hall term is excluded from Eq. (1), as it is small in comparison with fluid convection: $(\frac{d_i}{L})(\frac{v_A}{v}) \ll 1$ (where the length scale can be $L \sim L_T = T_e/\nu\nabla T_e$, the temperature scale length; $d_i = c/\omega_{\mathrm{pi}}$ is the ion skin depth). Because the plasma expansion velocities are supersonic and since $\beta \propto (c_s/v_A)^2 \gg 1$, the velocities are also superalfvenic, and thus, the Hall term is insignificant.

Theoretical modeling by Haines [5,20] and numerical simulation by Schoeffler *et al.* [18,19] laid a universal diagram of saturated magnetic field vs the normalized length scale, as illustrated in Fig. 1, indicating different physical regimes from the resistive ($L_{\mathrm{T}}/d_i \gtrsim 1$) to the convective ($L_{\mathrm{T}}/d_i \gtrsim 1$) and a kinetic regime where kinetic instabilities contribute to field generation ($L_T/d_i \gg 1$). For typical HED plasmas, fluid convection dominates the structure and dynamics of the magnetic field when the normalized temperature gradient length scale L_T/d_i is greater than unity. Considering the magnetic fields frozen in the plasma and convected with the plasma

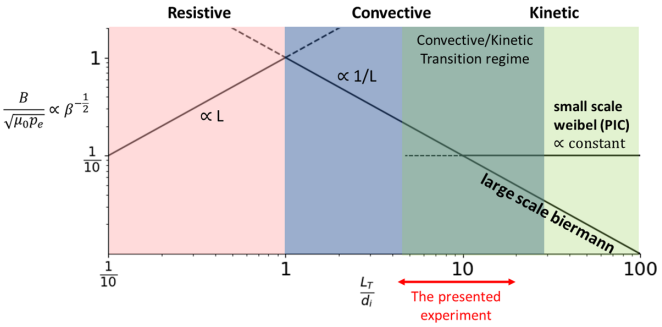

FIG. 1. Universal diagram of normalized, saturated magnetic fields ($\propto \beta^{-1/2}$) vs the normalized length scale (L_T/d_i) plotted at different regimes from the resistive ($L_T/d_i \lesssim 1$) to the convective ($L_T/d_i \gtrsim 1$) [5,20] and the kinetic ($L_T/d_i >> 1$) [18,19]. Note that the ratio of specific heats is taken to be 1 because the electrons are isothermal. The presented experiments are in the transition region from convective to kinetic ($L_T/d_i \sim$ 5-20).

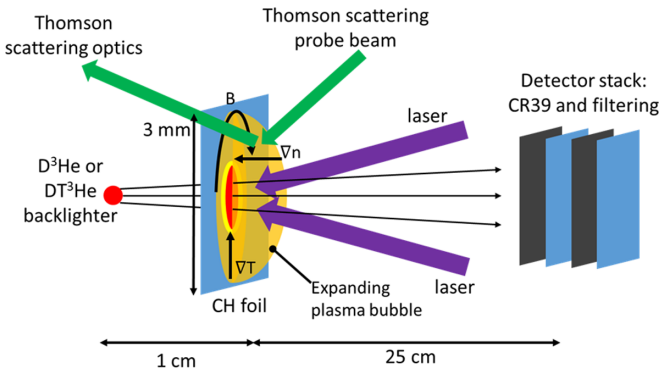

FIG. 2. Schematic diagram of experiment setup. The CH foil is driven by several OMEGA laser beams, with 2 kJ total energy. A charged particle backlighter is driven by the remaining beams of the OMEGA laser. Monoenergetic fusion products with an approximately uniform spatial distribution [20] from the backlighter stream through the plasma where they are deflected by fields and scattering and then are recorded on a CR-39 detector. The fluence of charged particles on the detector encodes the spatially resolved deflection field experience by the particles in the plasma, allowing for the line-integrated magnetic field to be inferred [8,23].

flow ($\mathbf{v} \times \mathbf{B}$) with an approximate expansion velocity, i.e., $v \approx C_s$, the balance of convective loss with the generation of Biermann field leads to [5,20]

$$B = \frac{1}{L_T}\sqrt{\frac{m_i k T_e}{Ze^2}}. \tag{2}$$

This scaling is consistent with predictions by particle-in-cell simulations [18,19]. While previous laboratory experimenters have observed magnetic fields and used simulations to argue the relevant mechanisms in field generation and transport [8,11,21,22], no experimenters have systematically measured the scaling of normalized field strengths as a function of system length scale. Theoretical and numerical modeling have provided useful insight into the saturation mechanisms, but experimental demonstration remains elusive and largely as speculation. Among many difficulties still in controlled laboratory experiments, creating plasmas with the relevant parameter range and scales in a unique physics regime is an extremely difficult undertaking. In addition, diagnosing and quantitatively characterizing the plasmas and magnetic fields is quite challenging, requiring advanced techniques that were previously limited. Consequently, authors of previous work often focused on single-shot experiments, lacking a coverage of the spatially and temporally resolved dynamics of the saturated magnetic fields in a relevant physics regime.

In this letter, we report an experiment on the dynamics and scaling of the saturation of spontaneously generated magnetic fields in laser-produced, high-thermal-β HED plasmas. The experiments, using state-of-the-art diagnostics such as charged-particle radiography [8,23] and time-resolved Thomson scattering [24,25], have provided quantitative information to model the field saturation in convection-dominated plasmas.

The spatially resolved magnetic fields are numerically reconstructed from proton radiography data, leading to a quantitative physics picture of field saturation with a scaling of $B \sim 1/L_T$ for a convectively dominated plasma, a regime where the temperature gradient scale length modestly exceeds the ion skin depth ($L_T/d_i > 1$).

The experiments were conducted on the 60-beam, 30-kJ OMEGA laser [26]. Figure 2 depicts the schematic experimental setup. The subject plasma is generated as laser drive beams impinge on a 25-μm-thick polystyrene (CH) foil. The 351 nm wavelength laser drive is in one of two configurations: 2 (or 1) TW of laser power distributed among four (or six) 500-J beams, with 1 (or 3) ns duration. Each beam utilized a phase plate to uniformly distribute the pulse energy over a super-Gaussian spot with radius 400 μm. An implosion-based charged-particle backlighter filled with a deuterium-tritium-helium-3 gas mixture (DT^3He) [20] was driven with 40 of the beams. Relative timing between backlighter and the subject laser drives was adjusted to probe the subject at different times. Particles are produced over a duration of $\lesssim$ 100 ps [23], dictating the temporal resolution of the radiography system, and the probe times are chosen to be between 0.2 and 2.5 ns after the start of the subject drive. Figures 3(a)–3(c) show some of the monoenergetic charged-particle radiographs taken at different times with 3-MeV protons, 9.5-MeV deuterons, and 15-MeV protons, products of the $d + d \rightarrow {}^3\mathrm{H} + p(3\,\mathrm{MeV})$, $t + {}^3He \rightarrow {}^4\mathrm{He} + d(9.5\,\mathrm{MeV})$, and $d + {}^3\mathrm{He} \rightarrow {}^4\mathrm{He} + p(14.7\,\mathrm{MeV})$ reactions, respectively [23].

Shown in Figs. 3(d)–3(f), the corresponding spatially resolved magnetic fields are reconstructed with an advanced algorithm [27–30], allowing for the quantification of the details of magnetic field distribution and strength. The algorithm solves for the optimal transport of the initial particle flux to the observed particle flux (as recorded by the radiograph) outputting a spatially resolved deflection field. Under the assumption that the dominant mechanism for deflection is the magnetic component of the Lorentz force, the magnetic field is then retrieved. This technique for interpreting

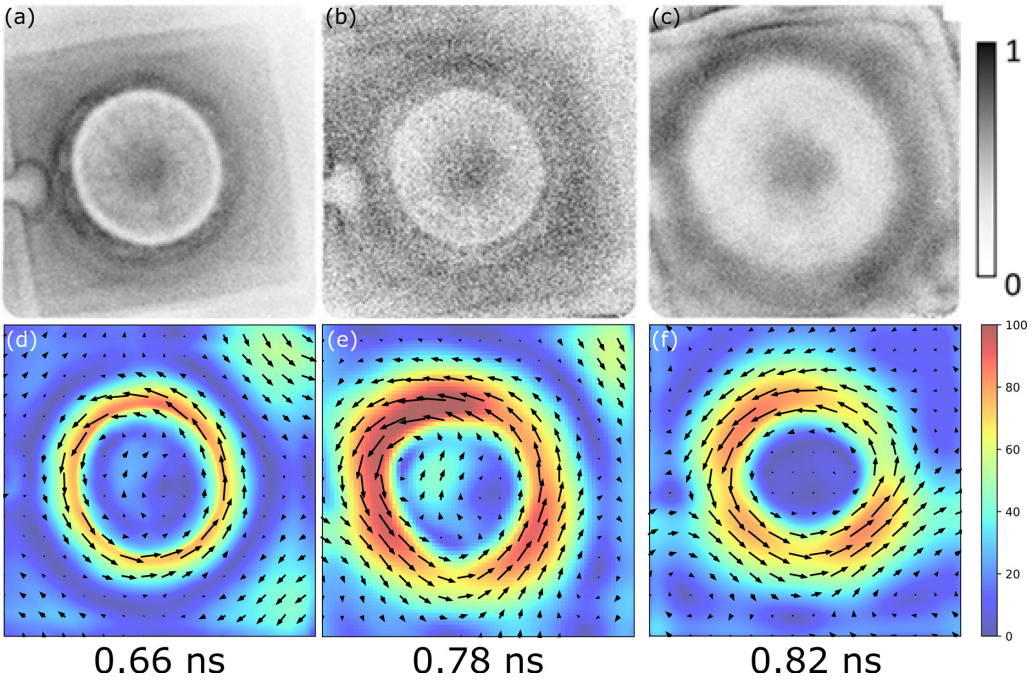

FIG. 3. (a)–(c) Charged particle radiography data and (d)–(f) numerical magnetic field reconstructions from a representative shot (OMEGA shot 95103). Data are arranged in columns by particle species: (a) and (d) D^3He protons, (b) and (e) T^3He deuterons, and (c) and (f) DD protons. The units and colormap for the reconstructions are the same for all three reconstructions, which show the path-integrated magnetic field in MG·μm. Radiograph detectors are 10 × 10 cm squares, corresponding to a 4 × 4 mm field of view at the plasma subject and are normalized to the maximum measured particle fluence, which differs by particle species. The average particle fluences are $3.5 \times 10^4/\text{cm}^2$, $4.9 \times 10^3/\text{cm}^2$, and $1.3 \times 10^4/\text{cm}^2$ for the D^3He protons, T^3He deuterons, and DD protons, respectively. In the radiograph, dense (sparse) regions imply an accumulation (rarefaction) of particles which are interpreted into a spatially resolved map of particle deflections through an algorithm solving for optimal transport of the particles. The variation between magnetic field maps measured by each particle depends somewhat on time-of-flight evolution between particles and the degree to which deflections are not caused by magnetic fields. Scattering in plasma, for example, leads to the additional blurring in feature sizes, (c) and (f) particularly the DD-proton radiograph and reconstruction, (b) and (e) while low statistics contribute to the lack of feature sharpness in the T^3He deuteron radiograph and reconstruction. Because blurring from scattering in the DD-proton images is much stronger than in the other radiographs, the peak magnetic fields from DD protons are not used in the final scaling analysis but still provide corroboration of plasma bubble expansion velocity.

charged-particle radiography data is becoming commonplace [16,17,31–34].

It is important to point out that the self-generated spontaneous electric field in these proton images can be largely ignored. In earlier experiments, in which protons in a face-on geometry probed Biermann-generated fields simultaneously in both parallel and antiparallel directions [35–37], authors quantitatively demonstrated that the deflections of protons in a face-on probe geometry are insensitive to the electric field.

Several characteristic features shown in the reconstructed images include, first, the circulating Biermann fields which are concentrated in the edge of the plasma bubble, a consequence of the large temperature gradients occurring at the bubble edge, and second, that the fields are convected with the plasma bubble expansion, suggesting fluid convection dominating the field transport and indicating the physics processes described in Eq. (1) are sufficient to explain the data to the first order. Considering a typical particle probe pathlength approximately equal to the bubble shell thickness with ∼100 μm, the peak values of the inferred magnetic fields from these images [Figs. 3(d)–3(f)] are extracted and plotted as a function of time in Fig. 4. It is shown that, in the period until ∼0.6 ns, the magnetic field grows rapidly because of the quick plasma heating and large gradients while the laser drive is on. The continuous increase in plasma temperature and plasma bubble expansion leads to the formation of large temperature gradient (∇T_e) and density gradient (∇n_e), resulting in magnetic field generation ($\nabla n_e \times \nabla T_e$) which exceeds the field convection. In the meantime, the increasing temperature results in the reduction of the plasma resistivity, and therefore, the resistive dissipation of fields is negligible. At the time ∼0.6 ns, the magnetic fields reach their peak value and turn to decay as the overshooting field is balanced by the field transport through convection. As the plasma bubble accelerates (up to ∼1000 km/s, as seen in proton radiographs and FLASH hydrodynamic simulations [38,39] with parameters matching the experiment), the enhanced field convection balances the field generation in the times of ∼1.0–2.5 ns, eventually reaching a quasi-equilibrium [$\nabla n_e \times \nabla T_e / e n_e \sim \nabla \times (\mathbf{v} \times \mathbf{B})$], where the measured field strength saturates. The physics processes are taking place on hydrodynamic timescales (subnanosecond) consistent with convection mechanisms.

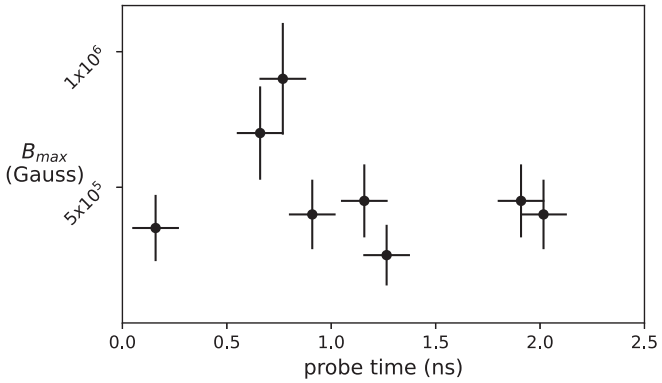

FIG. 4. Time evolution of the peak magnetic field inferred from each of the shots in the ensemble. The peak magnetic field is obtained by azimuthally averaging the reconstructed path-integrated magnetic field maps and choosing the largest value. To convert path-integrated field to field, the transverse length over which the field exists is assumed to be 100 μm, a scale corroborated by simulations and previous experiments in the same geometry [11]. In early measurements (0–0.6 ns), plasma conditions have large gradients (and thus Biermann source term), and the magnetic field rapidly grows until it reaches a peak and then decays (0.6–1.0 ns) as the overshooting field is balanced by the field transport, leading to reach a quasi-equilibrium and saturation (1.0–2.5 ns).

To quantify the spatially and temporally resolved plasma conditions, time-resolved 2ω Thomson scattering [8,25] measurements were conducted. In these measurements, the Thomson volume is a small cylinder ~100 μm long and 50 μm in diameter. Shown in Figs. 5(b) and 5(d) are the

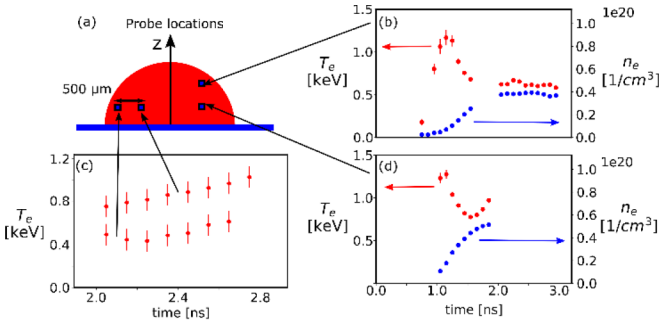

FIG. 5. Thomson scattering data at different locations in the plasma. The beam focus is ~800 μm in diameter. The three different measurement points (a single measurement point per shot) are laterally separated from the focus center by 1000, 1000, and 1500 μm and vertically separated from the foil surface by 500, 1000, and 500 μm, respectively. (b)–(d) Electron density (blue, right axis) and electron temperature (red, left axis) are extracted from the electron plasma wave contribution to the Thomson scattering spectrum. The temperature and density histories are collected in 1 ns streaks on separate shots; an example of evidence of shot-to-shot reproducibility can be seen in (b), where both the temperature and density traces are continuous despite the early time (0.8–1.8 ns) and late time (2.0–3.0 ns). (c) The measurement of temperature at two different locations, from which the temperature gradient scale length can be directly measured.

measured evolutions of electron temperature and density at different locations.

Furthermore, by performing Thomson scattering measurements at two selected locations separated by 500 μm distance perpendicular to the laser drive, the electron temperature gradient is directly measured. The values of the electron temperature and separation distance are used to extract the temperature gradient as a function of time, which is found to be 750 ± 150 μm and is largely time independent. This scale length is to be expected, as it is of a similar order of the laser spot diameter (~800 μm), and it is the laser which imposes the temperature gradient.

The data are converted to normalized quantities for the sake of comparison with theoretical predictions. The magnetic field, as measured by proton radiography, is normalized to the plasma pressure measured by electron plasma wave Thomson scattering. The temperature gradient length scale is normalized to the ion inertial length, both measured by Thomson scattering. The proton radiography measurements of peak magnetic field do not happen exactly when and where the Thomson scattering measurements are taken. To make the analysis simulation agnostic, a simple model was constructed to extrapolate the Thomson measurements away from the probe locations. For each data point in normalized quantity space, the location and measurement time of the peak magnetic field are extracted from proton radiography. The Thomson scattering data are interpolated at that location and time using a model of the plasma bubble evolution. The model uses the bubble velocity as observed in proton radiography to self-consistently relate the arrival time of Thomson data features at the Thomson probe location to radiography locations. The model is as follows:

$$n(r,t) = n_{\mathrm{TS}}\left(t - \frac{r - r_{\mathrm{TS}}}{v_b}\right)\left(\frac{r_{\mathrm{TS}}}{r}\right)^{\gamma_n}, \tag{3}$$

$$T(r,t) = T_{\mathrm{TS}}\left(t - \frac{r - r_{\mathrm{TS}}}{v_b}\right)\left(\frac{r_{\mathrm{TS}}}{r}\right)^{\gamma_T}, \tag{4}$$

where the parameters are the bubble velocity v_b, the exponent relating density measurements at different points γ_n, and the exponent relating temperature measurements at different points γ_T. The position of the Thomson volume is r_{TS}. Because the Thomson data were collected at multiple locations, the exponents γ_n and γ_T are found by applying the model to the data of one location to transform it to the other location and tuning the exponent until both datasets match. The values of v_b are found to be ~300 and 1200 km/s from proton radiography data for the 1 and 2 TW laser power configurations, respectively. The exponents γ_n and γ_T are found to be 1.3 and 1.5 regardless of laser power. See Supplemental Material for further discussion of this model [40].

Figure 6 shows the normalized spontaneous magnetic field ($B/\sqrt{\mu_0 P_e} = \beta^{-1/2}$) as a function of the normalized temperature scale length (L_T/d_i) with a fit to a power law. It is shown that the Biermann field scales as $\beta^{-1/2} \sim (L_T/d_i)^{-0.71\pm0.47}$, in the regime with $L_T/d_i \sim$ 5-20. Given the uncertainty in the exponent of ±0.47, this value is consistent with the scaling predicted by theory [Eq. (2)] and particle-in-cell simulations [18,19], quantitatively demonstrating the saturation dynamics and scaling of the spontaneous magnetic field due to

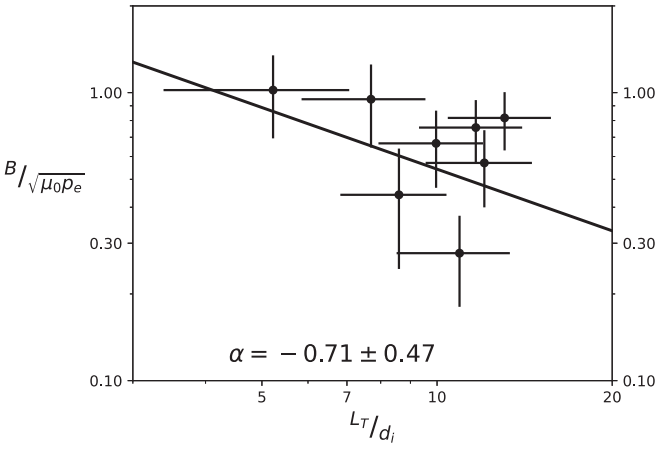

FIG. 6. The normalized magnetic field ($\tilde{B} \propto \beta^{-1/2}$) vs the normalized length scale ($\tilde{L} \sim L_T/d_i$) is plotted with the best fit to a model $\tilde{B} = A\tilde{L}^{\alpha}$ (black solid line). The fit is consistent with a relation of $B \sim 1/L_T$ within uncertainty, indicating that convection is dominant process of field saturation as predicted by the theoretical modeling [5] and numerical simulation [18,19].

plasma convection in a high-thermal-β, laser-produced HED plasma.

That the measured exponent ($\sim -0.71 \pm 0.47$) deviates from unity in this set of experiments is attributed to the plasmas being in a transition region between different regimes (from convective to kinetic), as shown in Fig. 1 with $L_T/d_i \sim$ 5-20. In this transition regime, magnetic fields are generated by both large-scale Biermann effects and small-scale kinetic instabilities, such as electron Weibel instability [18,19], and consequently, the scaling is some combination of the Biermann-convective saturation ($B \propto L_T^{-1}$) and the saturated Weibel scaling ($B \propto L_T^0$).

In summary, we have performed experiments to quantitatively demonstrate the scaling of the spontaneous large-scale Biermann magnetic fields in laser-produced HED plasmas. We have shown that, in the regime, with normalized scale length $L_T/d_i > 1$, the observed saturation scaling is consistent with $B \sim 1/L_T$, the scaling which predictions by theoretical modeling and particle-in-cell simulations show would result from the balancing of Biermann fields by fluid convection. In this letter, we provide confirmation of the physical insight into the fundamental physics of magnetic field saturation in plasmas and motivate further study of field saturation in broader regimes, such as turbulence/resistively dominated regimes with $L_T/d_i \lesssim 1$ and kinetic regimes with $L_T/d_i \gg 1$ where other magnetic field generation mechanisms can play a role.

This letter was supported in part by the U.S. Department of Energy (DOE)/National Nuclear Security Administration (NNSA) Centers of Excellence Contract No. DE-NA0003868, National Laser Users' Facility Contract No. DE-NA0003938.

[1] E. G. Zweibel and C. Heiles, Nature **385**, 131 (1997).
[2] R. M. Kulsrud and E. G. Zweibel, Rep. Prog. Phys. **71**, 046901 (2008).
[3] J. A. Stamper, K. Papadopoulos, R. N. Sudan, S. O. Dean, E. A. McLean, and J. M. Dawson, Phys. Rev. Lett. **26**, 1012 (1971).
[4] A. Raven, O. Willi, and P. T. Rumsby, Phys. Rev. Lett. **41**, 554 (1978).
[5] M. G. Haines, Phys. Rev. Lett. **78**, 254 (1997).
[6] L. Biermann and A. Schlüter, Phys. Rev. **82**, 863 (1951) .
[7] M. A. Yates, D. B. van Hulsteyn, H. Rutkowski, G. Kyrala, and J. U. Brackbill, Phys. Rev. Lett. **49**, 1702 (1982).
[8] M. Borghesi, A. J. MacKinnon, A. R. Bell, R. Gaillard, and O. Willi, Phys. Rev. Lett. **81**, 112 (1998).
[9] U. Wagner, M. Tatarakis, A. Gopal, F. N. Beg, E. L. Clark, A. E. Dangor, R. G. Evans, M. G. Haines, S. P. D. Mangles, P. A. Norreys *et al.*, Phys. Rev. E **70**, 026401 (2004).
[10] P. M. Nilson, L. Willingale, M. C. Kaluza, C. Kamperidis, S. Minardi, M. S. Wei, P. Fernandes, M. Notley, S. Bandyopadhyay, M. Sherlock *et al.*, Phys. Rev. Lett. **97**, 255001 (2006).
[11] C. K. Li *et al.*, Phys. Rev. Lett. **97**, 135003 (2006).
[12] C. K. Li, F. H. Séguin, J. A. Frenje, M. Rosenberg, R. D. Petrasso, P. A. Amendt, J. A. Koch, O. L. Landen, H. S. Park, H. F. Robey *et al.*, Science **327**, 1231 (2010).
[13] R. Betti and O. A. Hurricane, Nature Phys. **12**, 435 (2016).
[14] G. Gregori, A. Ravasio, C. D. Murphy, K. Schaar, A. Baird, A. R. Bell, A. Benuzzi-Mounaix, R. Bingham, C. Constantin, R. P. Drake *et al.*, Nature (London) **481**, 480 (2012).
[15] C. K. Li, P. Tzeferacos, D. Lamb, G. Gregori, P. A. Norreys, M. J. Rosenberg, R. K. Follett, D. H. Froula, M. Koenig, F. H. Seguin *et al.*, Nature Comm. **7**, 13081 (2016).
[16] P. Tzeferacos, A. Rigby, A. F. A. Bott, A. R. Bell, R. Bingham, A. Casner, F. Cattaneo, E. M. Churazov, J. Emig, F. Fiuza *et al.*, Nature Comm. **9**, 591 (2018).
[17] C. K. Li, V. T. Tikhonchuk, Q. Moreno, H. Sio, E. D'Humières, X. Ribeyre, Ph. Korneev, S. Atzeni, R. Betti, A. Birkel *et al.*, Phys. Rev. Lett. **123**, 055002 (2019).
[18] K. M. Schoeffler, N. F. Loureiro, R. A. Fonseca, and L. O. Silva, Phys. Rev. Lett. **112**, 175001 (2014).
[19] K. M. Schoeffler, N. F. Loureiro, R. A. Fonseca, and L. O. Silva, Phys. Plasmas **23**, 056304 (2016).
[20] M. G. Haines, Canadian J. of Phys. **64**, 912 (1986).
[21] L. Gao, P. M. Nilson, I. V. Igumenshchev, M. G. Haines, D. H. Froula, R. Betti, and D. D. Meyerhofer, Phys. Rev. Lett. **114**, 215003 (2015).
[22] P. T. Campbell, C. A. Walsh, B. K. Russell, J. P. Chittenden, A. Crilly, G. Fiksel, P. M. Nilson, A. G. R. Thomas, K. Krushelnick, and L. Willingale, Phys. Rev. Lett. **125**, 145001 (2020).
[23] G. D. Sutcliffe, P. Adrian, J. Pearcy, T. Johnson, N. Kabadi, S. Haque, C. Parker, B. Lahmann, J. Frenje, M. Gatu-Johnson *et al.*, Rev. Sci. Instrum. **92**, 063524 (2021).
[24] D. H. Froula, S. H. Glenzer, N. C. Luhmann Jr., and J. Sheffield, *Plasma Scattering of Electromagnetic Radiation* 2nd Ed. (Elsevier, Oxford, 2011).
[25] M. J. Rosenburg, J. S. Ross, C. K. Li, R. P. J. Town, F. H. Séguin, J. A. Frenje, D. H. Froula, and R. D. Petrasso, Phys. Rev. E **86**, 056407 (2012).

[26] J. M. Soures, R. L. McCrory, C. P. Verdon, A. Babushkin, R. E. Bahr, T. R. Boehly, R. Boni, D. K. Bradley, D. L. Brown, R. S. Craxton *et al.*, Phys. Plasmas **3**, 2108 (1996).

[27] A. F. A. Bott, C. Graziani, P. Tzeferacos, T. G. White, D. Q. Lamb, G. Gregori, and A. A. Schekochihin, J. Plasma Phys. **83**, 90580614 (2017).

[28] M. M. Sulman, J. F. Williams, and R. D. Russell, Appl. Numer. Math. **61**, 298 (2011).

[29] N. L. Kugland, D. D. Ryutov, C. Plechaty, J. S. Ross, and H.-S. Park, Rev. Sci. Instrum **83**, 101301 (2012).

[30] C. Graziani, P. Tzeferacos, D. Q. Lamb, and C. Li, Rev. Sci. Instrum. **88**, 023507 (2017).

[31] L. E. Chen, A. F. A. Bott, P. Tzeferacos, A. Rigby, A. Bell, R. Bingham, C. Graziani, J. Katz, M. Koenig, C. K. Li *et al.*, Astrophys. J. **892**, 114 (2020).

[32] A. F. A. Bott, P. Tzeferacos, L. Chen, C. A. J. Palmer, A. Rigby, A. R. Bell, R. Bingham, A. Birkel, C. Graziani, D. H. Froula *et al.*, Proc. Natl. Acad. Sci. USA **118**, e2015729118 (2021).

[33] W. Fox, D. B. Schaeffer, M. J. Rosenberg, G. Fiksel, J. Matteucci, H.-S. Park, A. F. A. Bott, K. Lezhnin, A. Bhattacharjee, D. Kalantar *et al.*, arXiv:2003.06351.

[34] J. Meinecke, P. Tzeferacos, J. S. Ross, A. F. A. Bott, S. Feister, H.-S. Park, A. R. Bell, R. Blandford, R. L. Berger, R. Bingham *et al.*, Sci. Adv. **8**, eabj6799 (2022).

[35] R. D. Petrasso, C. K. Li, F. H. Seguin, J. R. Rygg, J. A. Frenje, R. Betti, J. P. Knauer, D. D. Meyerhofer, P. A. Amendt, D. H. Froula *et al.*, Phys. Rev. Lett. **103**, 085001 (2009).

[36] C. A. Cecchetti, M. Borghesi, J. Fuchs, G. Schurtz, S. Kar, A. Macchi, L. Romagnani, P. A. Wilson, P. Antici, R. Jung *et al.*, Phys. Plasmas **16**, 043102 (2009).

[37] G. Sarri, A. Macchi, C. A. Cecchetti, S. Kar, T. V. Liseykina, X. H. Yang, M. E. Dieckmann, J. Fuchs, M. Galimberti, L. A. Gizzi *et al.*, Phys. Rev. Lett. **109**, 205002 (2012).

[38] B. Fryxell, K. Olson, P. Ricker, F. X. Timmes, M. Zingale, D. Q. Lamb, P. MacNeice, R. Rosner, J. W. Truran, and H. Tufo, Astrophys. J. **131**, S273 (2000).

[39] P. Tzeferacos, M. Fatenejad, N. Flocke, C. Graziani, G. Gregori, D. Q. Lamb, D. Lee, J. Meinecke, A. Scopatz, and K. Weide, High Energy Density Phys. **17**, 24 (2015).

[40] See Supplemental Material at http://link.aps.org/supplemental/10.1103/PhysRevE.105.L063202 for further discussion of the Thomson scattering interpolation model.